processes

MDPI

Article

Optimization of Key Parameters of the Air Distributor for the KYF Flotation Machine

Chao Lv [1,2,*], Ning Wei [1], Hongliang Zhao [3,*], Ming Wang [1], Hanwen Zhang [1] and Hongru Qiu [1]

[1] School of Control Engineering, Northeastern University at Qinhuangdao, Qinhuangdao 066004, China; wein@mails.neu.edu.cn (N.W.); wangm8@mails.neu.edu.cn (M.W.); zhanghanwen@mails.neu.edu.cn (H.Z.); qiuhongru@mails.neu.edu.cn (H.Q.)
[2] State Key Laboratory of Mineral Processing, BGRIMM Technology Group, Beijing 100160, China
[3] School of Metallurgical and Ecological Engineering, University of Science and Technology Beijing, Beijing 100083, China
* Correspondence: lvchao@neuq.edu.cn (C.L.); zhaohl@ustb.edu.cn (H.Z.)

Abstract

With the decreasing availability of high-quality mineral resources and the increasing complexity of ore properties, efficient and sustainable flotation technology has become a research focus in the field of mineral processing. To optimize the taper angle of the air distributor in a KYF flotation machine, numerical simulation was used in this study to investigate its influence on the internal flow field, gas-phase characteristics, structural pressure distribution, and stirring power consumption. The results show that the peak turbulent kinetic energy and gas holdup are concentrated in the shear zone between the impeller and stator. Under the +5° condition, the peak turbulent kinetic energy is the lowest, while its vertical distribution is the most uniform. The peak gas holdup in the impeller–stator region reaches 19.2%, and the number of efficient bubbles with a diameter of 0.5 mm reaches 3.8×10^6 per m^3, which is significantly higher than under the other conditions. During stable operation, this condition exhibits the lowest stirring power consumption at 126.0 W, which is 7.557% and 4.255% lower than under the −5° and 0° conditions, respectively. The optimal taper angle is therefore determined to be +5°. However, the associated large pressure gradient on the impeller surface may accelerate blade wear, indicating that surface strengthening measures should be considered to balance performance and durability.

Keywords: KYF flotation machine; air distributor; computational fluid dynamics; population balance model; bubble size

Check for updates

Academic Editor: Blaž Likozar

Received: 26 March 2026
Revised: 10 April 2026
Accepted: 13 April 2026
Published: 15 April 2026

Copyright: © 2026 by the authors. Licensee MDPI, Basel, Switzerland. This article is an open access article distributed under the terms and conditions of the Creative Commons Attribution (CC BY) license.

1. Introduction

Minerals are the core raw materials for industrial production, providing a solid foundation for the stable operation of multiple fields such as metallurgy and chemical engineering. The beneficiation process is a crucial step in achieving the efficient utilization of mineral resources [1,2]. Among these processes, flotation, as the mainstream beneficiation method, directly determines the efficiency and accuracy of mineral separation and serves as the core step in the beneficiation process [3,4]. Currently, mineral resources are becoming increasingly lean, fine-grained, and complex, and the performance of traditional mineral processing equipment can no longer meet the requirements for high efficiency, energy saving, and stable separation. Consequently, there is an urgent need to independently develop high-end mineral processing equipment and to optimize the structure of key components,

in order to elevate the level of mineral processing technology [5]. As the core equipment of the flotation process, the performance of a flotation machine directly affects the mineral processing indices. The KYF flotation machine, a typical forced-air mechanical agitation flotation machine, was jointly developed by BGRIMM Technology Group and domestic research institutions. This equipment operates by combining external forced aeration with mechanical agitation. The rotation of the impeller drives slurry circulation and generates intense turbulence, allowing air to be fully sheared and dispersed into fine and uniform bubbles, thereby improving the collision and attachment efficiency between minerals and bubbles. Its tank is mostly of a U-shaped configuration, which effectively reduces sanding and slurry short-circuiting, enhancing separation stability. Owing to its excellent mineral processing performance and high reliability, this equipment has been widely applied in the separation of non-ferrous metals, non-metallic minerals, and other fields [6,7].

The internal flow field characteristics of flotation machines are the core factors determining flotation efficiency and mineralization effect. However, industrial-grade flotation cells have a large scale and complex internal flow field structure, and are subject to operating conditions that make accurate in situ monitoring difficult [8,9], which poses significant challenges for flow field analysis and equipment optimization. The development of Computational Fluid Dynamics (CFD) has provided an effective solution to this problem and has become an important means of simulating the flow field, predicting performance, and optimizing the structure of flotation machines [10–12]. Currently, a large number of scholars have conducted research on flotation machines using experiments and CFD technology:

Shi et al. [13–15] conducted systematic simulation and experimental research on key components of flotation machines. By optimizing the number and cross-sectional shape of stator blades in XCF flotation machines, they reduced energy consumption while maintaining performance. They also revealed the influence of stator blade thickness and axial clearance on the flow field of the KYF flotation machine, finding that blade thickness dominates the dispersion of the liquid phase. In addition, they established a large-nozzle air-inflation device model to investigate the effects of inflation pressure and nozzle immersion depth on jet performance. Gao et al. [16] used laser Doppler anemometry (LDA) to study the effects of impeller diameter and bottom clearance on the bottom flow field of the KYF flotation machine. They found that a large-diameter impeller combined with a small bottom clearance can form a stable centripetal flow, effectively improving the suspension conditions of bottom particles, thereby providing an experimental basis for the structural optimization of flotation machine impellers. Xu et al. [17] designed an impeller with offset short blades. Compared with a conventional impeller, it effectively reduces the blockage caused by backflow vortices on the blade suction surface, enhances the effective flow passage and bubble cutting capability, and significantly increases the air intake, the number of medium- and fine-sized bubbles, as well as the gas holdup and gas dispersion in the flotation cell. Li [18] systematically analyzed the effects of impeller diameter, rotational speed, and blade inclination angle on the turbulent kinetic energy distribution and bubble dispersion state of the slurry, proposed an optimization scheme for impeller parameters under multi-objective constraints, improved the flow field stability, and enhanced the collision probability between mineral particles and bubbles. Niu et al. [19] employed the CFD Eulerian method to simulate the solid–liquid two-phase flow field in an XFD flotation machine, combined with hematite flotation experiments, to investigate the effects of impeller speed and particle size on the flow field distribution, fluid motion characteristics, and flotation kinetics of the flotation machine, and determined 1800 r/min as the optimal operating speed. Pan et al. [20] analyzed the internal flow field of a pneumatic microbubble flotation machine using CFD numerical simulation. By optimizing the layout and outlet structure of the microbubble generator, they effectively

reduced the rising speed of the slurry and bubbles, enhanced dispersion within the tank, and alleviated the overflow of tailings from the tank. Shen et al. [21–24] conducted systematic research on the large-scale and high-efficiency development of flotation equipment. They proposed an enlarged design method for inflatable self-priming flotation machines and successfully implemented the engineering application of 160 m^3 equipment. They also revealed the influence of operating parameters on the slurry suction performance and flow field of flotation machines, and developed a new type of impeller with optimized bubble distribution, significantly improving the recovery rate of coarse particles. Their research covers equipment scale-up, flow field analysis, and process optimization, providing support for the development of flotation equipment. Yu et al. [25] used the CFD Eulerian model to numerically simulate the XFD laboratory flotation machine. By optimizing the structure to modify the flow field pattern, they found that the adjusted flow field can enhance the turbulence intensity in the mixing zone and improve the velocity distribution of the three-phase flow at the bottom, thereby promoting bubble–particle collision and adhesion and effectively reducing the ash content of clean coal. Prakash et al. [26] systematically reviewed the hydrodynamic characteristics of flotation columns and the influence of key design parameters such as flow regime, gas holdup, and bubble size on separation efficiency. They also summarized relevant measurement techniques, providing an important reference for the design and optimization of flotation processes.

Based on existing research, most studies have focused on the structural improvement and parameter optimization of flotation machine impellers and stators to enhance stirring efficiency and flow field uniformity. In contrast, research on the design and optimization of air distributors remains relatively weak. As a key component for bubble generation and dispersion in flotation machines, the air distributor directly determines the initial distribution position of bubbles, which in turn affects the subsequent crushing, dispersion, and adhesion of bubbles to mineral particles [27,28], ultimately constraining the improvement of flotation performance. Therefore, conducting structural optimization research on the air distributor of the KYF flotation machine holds significant theoretical and engineering importance.

2. Research Methodology

2.1. Geometric Modeling and Meshing

This article takes the KYF inflatable mechanical agitation flotation machine as the research object and establishes its simulation model. The geometric model is shown in Figure 1 and mainly consists of the main shaft, impeller, air distributor, and stator. Among the components, the main shaft has a hollow structure and serves the dual functions of power transmission and air supply channel. The impeller adopts a backward-inclined conical structure, providing both good mixing capability and structural strength. The air distributor is a perforated cylindrical structure placed inside the impeller chamber to evenly distribute the airflow. The stator employs a suspended short-blade structure installed obliquely above the periphery of the impeller, which stabilizes the flow, suppresses swirl, and enhances bubble breakup. Existing KYF flotation machines typically use an air distributor with a standard 0° taper, as shown in Figure 2b. Based on the original structure, this study changes the taper angle of the air distributor and sets two additional conditions (−5° and +5°) for comparison with the original design, focusing on the variation patterns of the internal flow field structure, gas phase distribution, fluid pressure, and agitation power consumption of the flotation machine under different taper parameters. The remaining key structural dimensions of the flotation machine are kept consistent, with detailed parameters listed in Table 1.

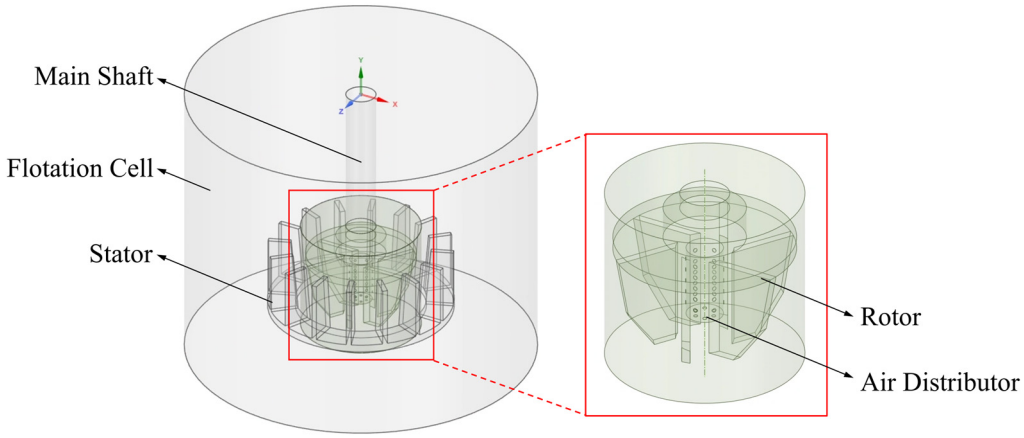

Figure 1. Schematic diagram of the geometric model of the flotation machine.

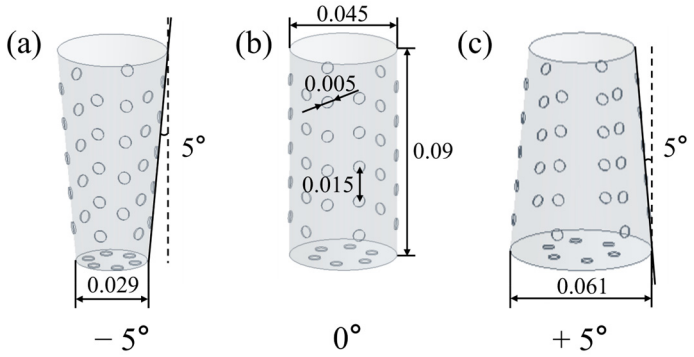

Figure 2. Schematic diagram of the air distributor taper angles: (**a**) −5°; (**b**) 0°; (**c**) +5°.

Table 1. Key structural dimensions of the flotation machine model.

Structure	Dimension/m	Structure	Dimension/m
Cell diameter	0.700	Stator outer diameter	0.370
Cell height	0.570	Stator inner diameter	0.260
Stirring shaft diameter	0.060	Stator blade height	0.120
Impeller diameter	0.220	Stator end plate thickness	0.015
Impeller height	0.140	Stator clearance from the bottom	0.090
Impeller blade thickness	0.010	Axial clearance	0.015

SpaceClaim (version 2024) was used to divide the fluid domain. The flotation cell was partitioned into two parts: the impeller rotating region and the stationary region. The impeller rotating region corresponds to the enlarged view in Figure 1. The physical model of the divided fluid domain was imported into Fluent Meshing (version 2024), and a polyhedral mesh was adopted for global mesh generation. Local mesh refinement was applied to key areas such as the impeller blades, stator blades, and air distributor orifices to improve simulation accuracy. We performed simulations on models with six different grid numbers: 80,000, 100,000, 120,000, 140,000, 160,000, and 200,000. The average liquid-phase velocities on the longitudinal section under each grid condition were compared, as shown in Table 2. The results indicate that the differences between the 120,000-grid model and the 140,000-, 160,000-, and 200,000-grid models are relatively small, with the relative errors controlled within 3%. Moreover, the 120,000-grid model has a smaller number of cells and thus lower computational cost. Therefore, this study adopts the 120,000-grid model for subsequent calculations, with the grid quality maintained above 0.8. The meshing result is shown in Figure 3.

Table 2. Comparison of average liquid-phase velocity on the longitudinal section under different grid numbers.

Number of Grid Cells ($\times 10^4$)	Average Liquid-Phase Velocity on the Longitudinal Section ($m \cdot s^{-1}$)	Relative Error (%)
8	0.317	−6.765
10	0.325	−4.412
12	0.336	−1.247
14	0.336	−1.176
16	0.338	−0.588
20	0.340	0

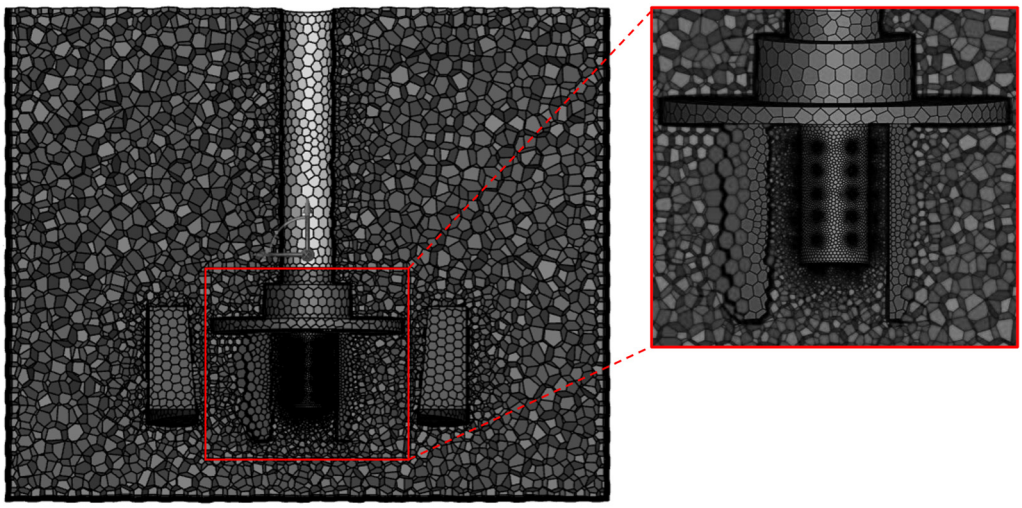

Figure 3. Mesh model of the flotation machine.

2.2. Boundary Conditions and Physical Parameters

Fluid simulation was conducted using Ansys Fluent (version 2024). Both the gas and liquid phases were set as continuous phases, with a surface tension of 0.072 N/m. The Eulerian multiphase model was selected, and the population balance model (PBM) was activated. A discrete method was employed for solving, with 10 bubble size bins, a ratio exponent of 4, and a minimum bubble diameter of 5×10^{-6} m. Bubble aggregation and breakage kernels were also activated to better match actual flotation conditions [29–31]. The Realizable k–ε model was used as the turbulence model, combined with standard wall functions to improve the accuracy of the near-wall flow field simulation. The boundary conditions were set as follows: the top of the flotation cell was set as a pressure outlet, with a relative static pressure of 0 Pa; the inlet boundary was defined as a velocity inlet, with an inlet velocity of 1 m/s. The initial size of the introduced bubbles corresponded to interval 4 (bin 4), with a diameter of approximately 5×10^{-4} m. The multiple reference frame (MRF) method was used to simulate the rotational motion of the impeller, with the impeller speed set at 250 rpm. A transient calculation method was employed to simulate the changes in the flow field inside the flotation cell, and the convergence residual was controlled below 10^{-3}. The time step was set to 0.01 s, and the total simulation duration was 120 s to fully capture the dynamic changes in the flow field and gas–liquid two-phase behavior within the flotation machine.

2.3. Model Validation

Comparing the motion trajectory of tracer particles with the simulated liquid-phase flow field structure is one of the commonly used methods to verify the accuracy of sim-

ulations [32]. Fan et al. [14] built a high-speed camera test system for particle motion, conducted physical experiments on flotation machines, and recorded the motion trajectories of tracer particles with the same density as water. Figure 4 shows the motion trajectories of four particles obtained from the experiment. Under the stirring effect of the impeller, two of the particles are ejected from the gap between the stator blades and move upward, eventually being sucked back into the upper part of the impeller; the other two particles are ejected from the gap between the stator blades and move downward, eventually being sucked back into the impeller region. Figure 5 shows the simulated streamline distribution from this study. It can be seen from the figure that the liquid-phase jet emitted from the gap between the stator blades reaches the tank wall and moves upward and downward, forming large-scale and small-scale circulation directed toward the impeller. Comparing the results in Figures 4 and 5, the spatial correspondence between the particle motion trajectories and the flow field structures validates the reliability of the simulation.

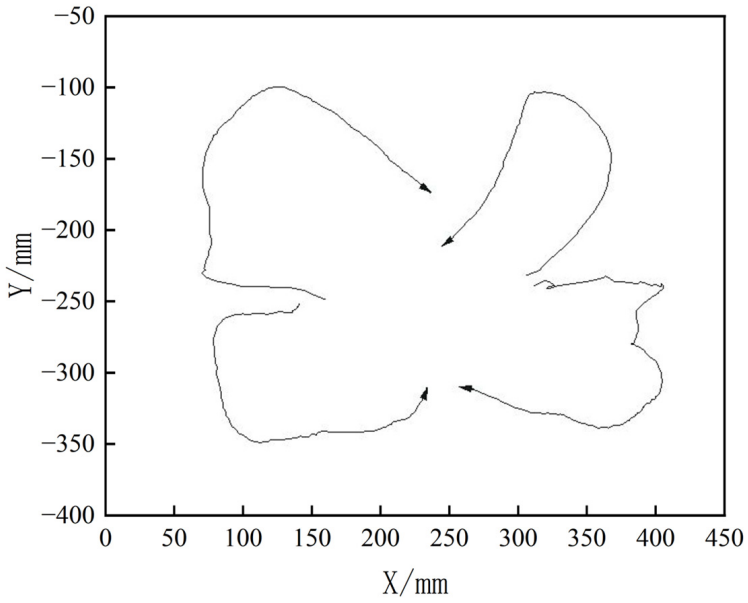

Figure 4. Motion trajectories of tracer particles from the experiment [14].

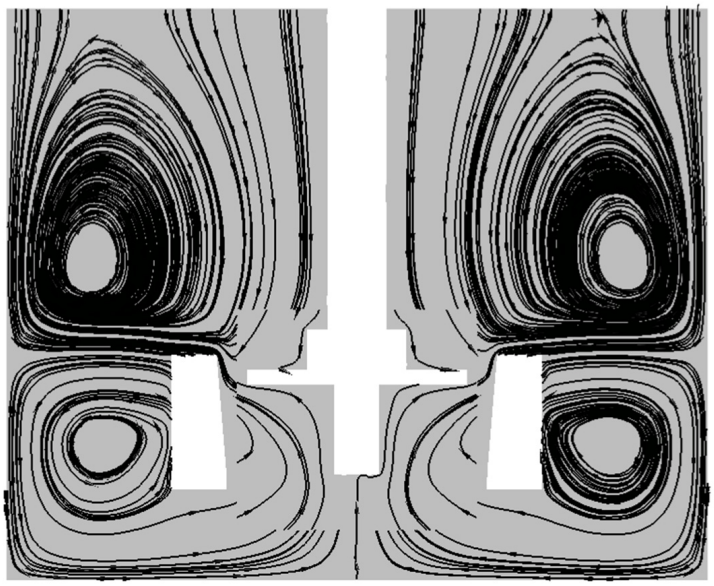

Figure 5. Simulated streamline distribution.

3. Results and Discussion

3.1. Flow Field Distribution Characteristics

Nine monitoring surfaces were selected for data extraction and analysis, including one longitudinal section and eight cross-sectional sections. The longitudinal monitoring surface passes through the axis of the mixing shaft, revealing the flow field structure along the height direction of the cell. The eight cross-sectional monitoring surfaces were selected sequentially along the height direction of the flotation cell at intervals of 0.05 m, starting from the bottom surface, to analyze parameters such as gas holdup and turbulent kinetic energy at different axial positions. Figure 6 shows a schematic diagram of each monitoring surface.

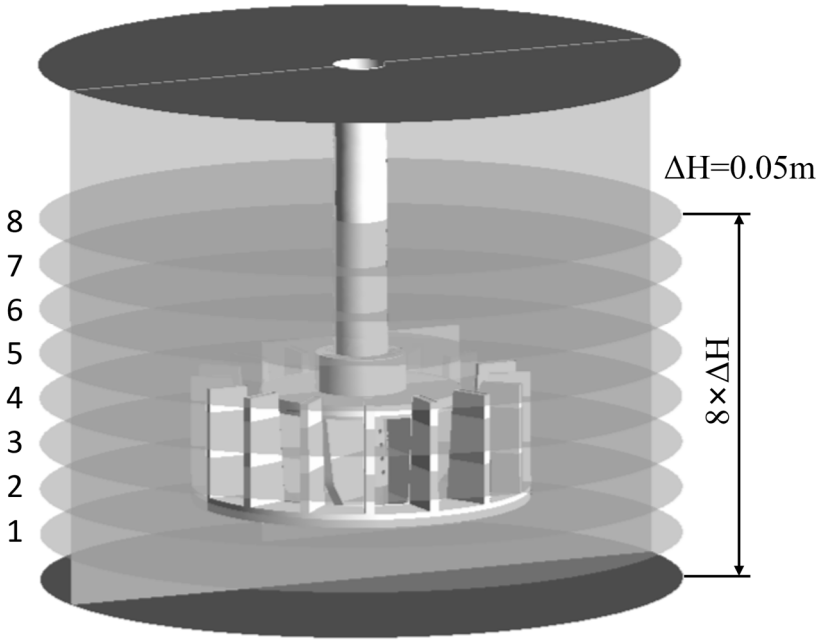

Figure 6. Schematic diagram of monitoring surfaces.

Analyzing the liquid-phase velocity contour and streamline plot reveals the flow field distribution, vortex, and dead zone characteristics, while the impeller circulation rate quantifies the pumping capacity of the impeller and the slurry circulation intensity. Together, they are used to evaluate the influence of the flow field structure on bubble dispersion and particle suspension performance. Figure 7 presents the liquid-phase velocity distribution contours and streamline plots on the longitudinal section under three taper angle conditions. Analysis of the velocity contours shows that the differences among the three conditions are minor, with similar velocity distribution characteristics, and the velocity in the impeller-stator core shear zone is relatively high. Examination of the streamline plots on the longitudinal section reveals that the streamlines are denser under the +5° condition, indicating a more compact flow field structure and more uniform flow coverage, which facilitates sufficient contact and dispersion of the gas–liquid two phases in the impeller-stator core zone. Under the three conditions of −5°, 0°, and +5°, the liquid volumetric flow rates at the outer cylindrical surface of the impeller are 0.074 m^3/s, 0.072 m^3/s, and 0.070 m^3/s, respectively. Although the volumetric flow rate under the +5° condition is slightly lower than those under the other two conditions, it does not lead to a significant decrease in circulation capacity, indicating that a larger circulation flow rate is not necessarily better, and further analysis is required in combination with other evaluation criteria.

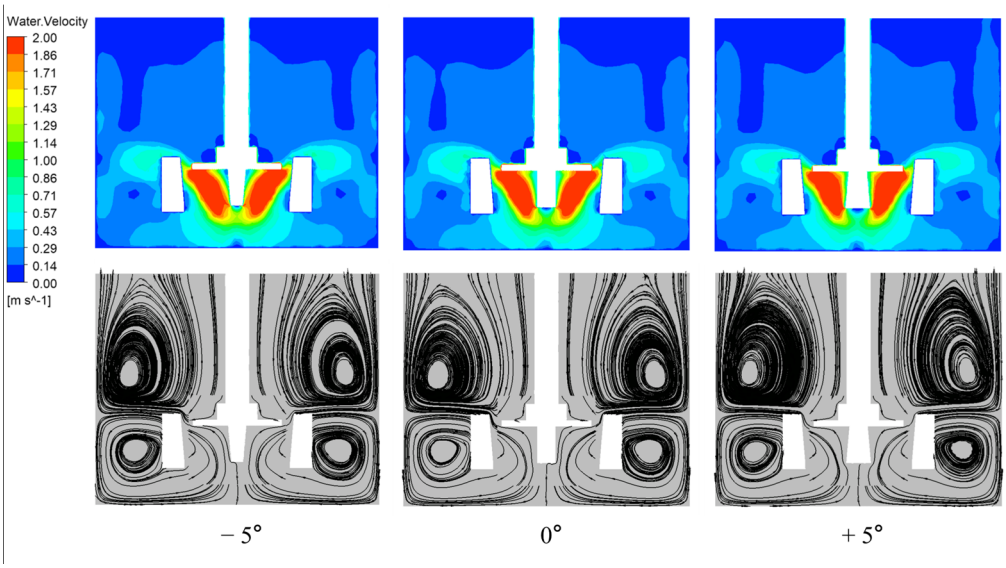

Figure 7. Liquid-phase velocity distribution contours and streamline plots on the longitudinal section under different taper angle conditions.

Turbulent kinetic energy is a key parameter that characterizes the intensity of fluid disturbance and turbulent mixing ability, and its spatial distribution directly reflects the stirring ability and energy transfer characteristics of the flow field. The distribution pattern of turbulent kinetic energy along the cell height under different taper conditions is shown in Figure 8. Since the impeller-stator core region is the location with the strongest shear action and the most concentrated energy input in the flow field, the peak turbulent kinetic energy under all three conditions appears in this region, where the intense turbulence directly drives bubble breakup and dispersion. In the lower and upper regions far from the agitation zone, the pumping and shear actions of the impeller are significantly weakened, leading to a rapid decrease in turbulent kinetic energy to a low level, accompanied by a substantial reduction in flow field disturbance. A comparison of the peak values shows that the highest turbulent kinetic energy peak occurs under the 0° condition, reaching 0.032 m^2/s^2, followed by the −5° condition with 0.02638 m^2/s^2, and the lowest under the +5° condition with 0.02435 m^2/s^2. This is mainly because the change in taper angle alters the flow channel shape and jet direction between the impeller and stator: under the 0° taper, the flow resistance is relatively low and the jet impact is more concentrated, resulting in the highest local turbulence intensity; whereas under the +5° taper, the flow field structure becomes more compact and the flow distribution more uniform, which, although reducing the peak intensity, leads to a gentler vertical decay of turbulent kinetic energy. Since turbulent kinetic energy is a key factor determining bubble breakup efficiency, an excessively high peak may cause over-breakage of bubbles, while an overly low peak is unfavorable for the dispersion of large bubbles. Therefore, it is necessary to further evaluate the matching degree between the flow field structure and bubble dispersion characteristics under each condition in combination with bubble size distribution.

3.2. Gas Phase Distribution Characteristics

Gas holdup is an important criterion for evaluating the uniformity of gas–liquid distribution and bubble residence time in flotation machines, as it determines the collision and attachment efficiency between mineral particles and bubbles. The distribution pattern of gas holdup along the cell height under different operating conditions is shown in Figure 9. Analysis shows that the gas holdup in the lower region far from the impeller–stator region is extremely low, resulting in low flow velocity and a poor gas–liquid mixing effect, which

is commonly characterized as the dead zone of the flow field. However, the gas holdup in the upper region far from the impeller–stator region remains stable at approximately 0.8% for all three operating conditions. The peak gas holdup values under the three operating conditions all occur in the impeller–stator region. The gas holdup values under the −5°, 0°, and +5° operating conditions are 11.2%, 14.1%, and 19.2%, respectively. Under the +5° taper condition, the peak gas holdup in the impeller–stator region is the highest, indicating the strongest gas–liquid dispersion capability. Consequently, the residence time of bubbles in the mixing zone is longer, which is more conducive to sufficient contact between mineral particles and bubbles.

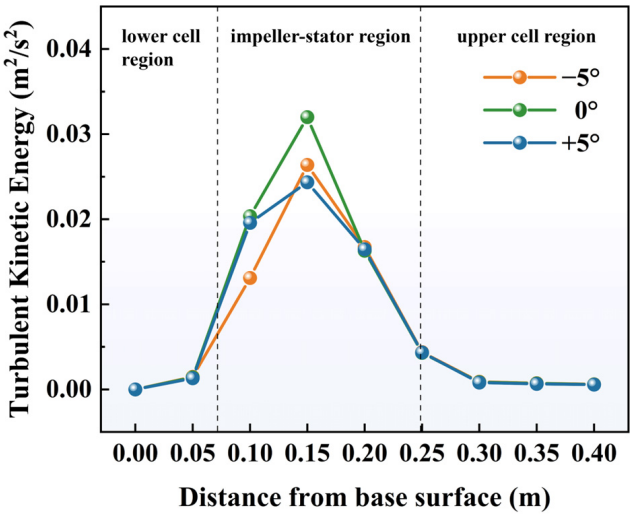

Figure 8. Distribution of turbulent kinetic energy along the cell height under different taper angles.

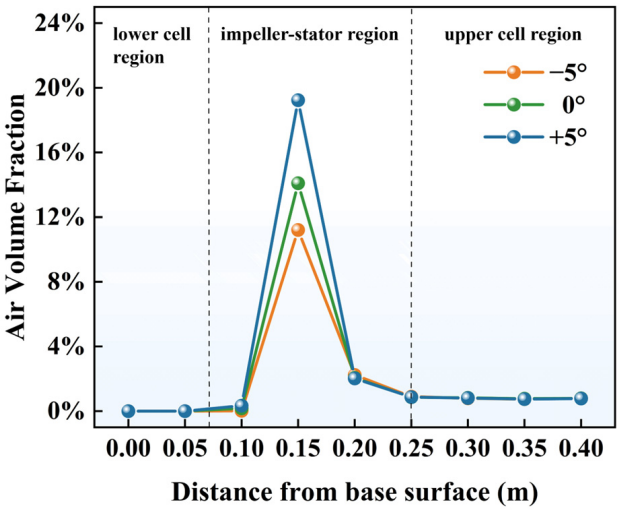

Figure 9. Distribution of gas holdup along the cell height under different taper angles.

However, analyzing only gas holdup has certain limitations. While an appropriate gas holdup can increase the gas–liquid interfacial area and the collision efficiency between particles and bubbles, an excessively high gas holdup can conversely lead to bubble coalescence, which in turn reduces the stability of the froth layer. Therefore, it is necessary to also consider bubble size distribution. In the flotation process, bubbles with a diameter ranging from 0.5 mm to 2 mm are generally considered efficient. These bubbles have a large specific surface area and a high rising speed, and are primarily responsible for the collision and attachment of mineral particles. Bubbles with a diameter of less than 0.2 mm are referred to as microbubbles; they possess an extremely high specific surface area but

lack sufficient upward kinetic energy and are highly prone to coalescence. Bubbles larger than 2.5 mm exhibit poor stability, ascend rapidly, and have a short residence time, making it difficult for them to effectively attach to mineral particles. These larger bubbles mainly serve to transport mineralized bubbles upward. Accordingly, we activated the PBM and selected ten bubble size bins (Bin 0 to Bin 9) for investigation. The specific bubble size parameters are listed in Table 3. The division of bubble diameter intervals is carried out using an iterative optimization method: the diameter range and the number of intervals are preliminarily set, followed by numerical simulation, after which ineffective intervals with scarce bubble counts are removed, and the interval parameters are then adjusted for recalculation. Through multiple simulation–correction cycles, a reasonable number and range of bubble diameter intervals are ultimately determined.

Table 3. Bubble size parameters.

Range		**>2.5 mm**		**0.5–2 mm**			**<0.2 mm**			
Bin	Bin 0	Bin 1	Bin 2	Bin 3	Bin 4	Bin 5	Bin 6	Bin 7	Bin 8	Bin 9
D/m	2×10^{-2}	8×10^{-3}	3×10^{-3}	1×10^{-3}	5×10^{-4}	2×10^{-4}	8×10^{-5}	3×10^{-5}	1×10^{-5}	5×10^{-6}

Figure 10 shows the number of bubbles per unit volume for different bubble diameters under the three operating conditions. For each operating condition, the bubble population is dominated by bubbles in the efficient size range of 0.5 mm to 2 mm, while the number of large bubbles larger than 2.5 mm remains at a relatively low level, indicating no significant bubble coalescence. Among them, bubbles with a diameter of approximately 0.5 mm exhibit a substantially higher number per unit volume than other sizes across all three conditions, constituting the dominant component of the bubble size distribution. The number of bubbles of this size under the −5°, 0°, and +5° conditions is 2.0×10^6, 2.4×10^6 and 3.8×10^6 respectively. Under the +5° condition, the number of efficient bubbles is significantly higher than under the other two conditions, indicating that it can form a more extensive gas–liquid interface in the impeller–stator region, which is conducive to improving the collision and attachment probability between mineral particles and bubbles. For large bubbles with a diameter greater than 2.5 mm, the numbers under the three operating conditions are similar and all remain at a low level, indicating that the shear of the flow field can effectively suppress the excessive generation of large bubbles under each operating condition. In the microbubble range (diameter less than 0.2 mm), the number of microbubbles under the 0° condition is relatively high, while that under the +5° condition is relatively low. This trend corresponds to the turbulent kinetic energy analysis results in Section 3.1. The peak turbulent kinetic energy under the 0° condition is the highest, and excessive breakup produces more microbubbles. In contrast, the turbulent kinetic energy under the +5° condition is evenly distributed with a moderate peak value, avoiding excessive bubble refinement and promoting efficient bubble formation. Furthermore, the combined results of gas holdup and bubble size distribution indicate that the high peak gas holdup under the +5° condition is mainly attributed to the sufficient dispersion of efficient small bubbles, rather than bubble coalescence. The gas holdup under this condition is within a reasonable range, and the gas–liquid dispersion behavior of the flow field is improved.

Figure 11 shows the volume fraction contours of bubbles with four different diameters (Bin 1 to Bin 4) in the flow field under the +5° operating condition. It can be seen that large bubbles exhibit a higher volume fraction and a wider distribution range. However, the previous PBM analysis results indicate that the number density of small bubbles is much higher than that of large bubbles. This is because the volume fraction reflects the spatial distribution of the gas phase volume. Although large bubbles are few in number,

the significant increase in gas phase volume contributed by each individual bubble means that under the same gas phase volume, more small bubbles can be generated. Therefore, the spatial distribution characteristics of the four bubble diameter groups were analyzed using volume fraction contours. From the distribution pattern, a conical region of low gas holdup is formed between the bottom of the flotation cell and the air distributor. This region exhibits low gas holdup, weak fluid disturbance intensity, and a limited gas–liquid mixing effect. Bin 1 bubbles have the widest distribution range, occupying a high volume fraction in the stator region, the outer zone of the stator, and the upper part of the cell. They serve as the main carrier for upward gas phase transport. As the bubble size decreases, the distribution range gradually shrinks. The efficient bubbles in the Bin 3 and Bin 4 diameter ranges are concentrated only at the outlet of the impeller air distributor and in the gap between the stator and impeller, indicating that the high turbulence intensity in this region effectively promotes bubble shear breakup and dispersion, generating a large number of fine bubbles and providing a sufficient gas–liquid interfacial area for bubble–particle collision and attachment.

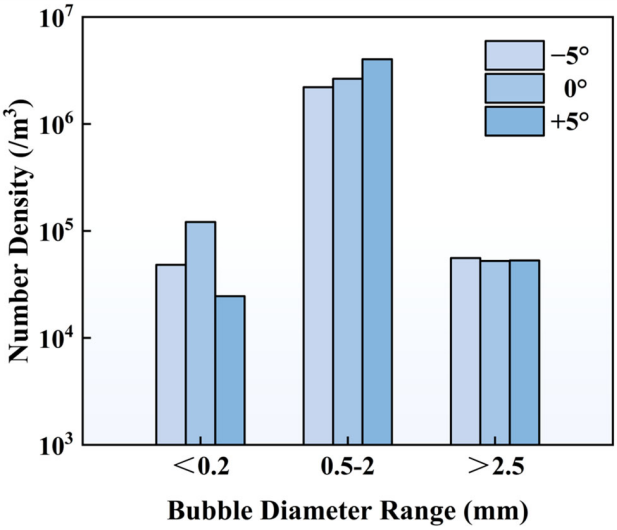

Figure 10. Number of bubbles per unit volume in different diameter ranges under different taper angles.

3.3. Power Consumption and Impeller-Stator Force Characteristics

The power of the stirring shaft is a core indicator that characterizes the energy input efficiency and operational economy of a flotation machine, and its magnitude directly reflects the fluid stirring intensity and energy consumption level. Analyzing the variation in shaft power under different operating conditions is crucial for improving the separation efficiency and energy conservation of flotation machines. Figure 12 shows the variation curves of power over time under different taper angles. Under all three operating conditions, an instantaneous power peak occurs during the start-up phase, followed by rapid decay. The dashed line in the figure marks the time point at which the power of the stirring shaft reaches a steady state, with the power stabilizing at approximately 3.5 s. During the stable operation phase, the power levels under the −5°, 0°, and +5° operating conditions are 136.3 W, 131.6 W, and 126.0 W, respectively. The +5° operating condition exhibits the best energy consumption performance, with reductions of 7.557% and 4.255% compared to the other two operating conditions, respectively. Under the premise of ensuring sufficient stirring intensity, lower energy consumption has been achieved, which better aligns with the design goal of high-efficiency and energy-saving flotation machines.

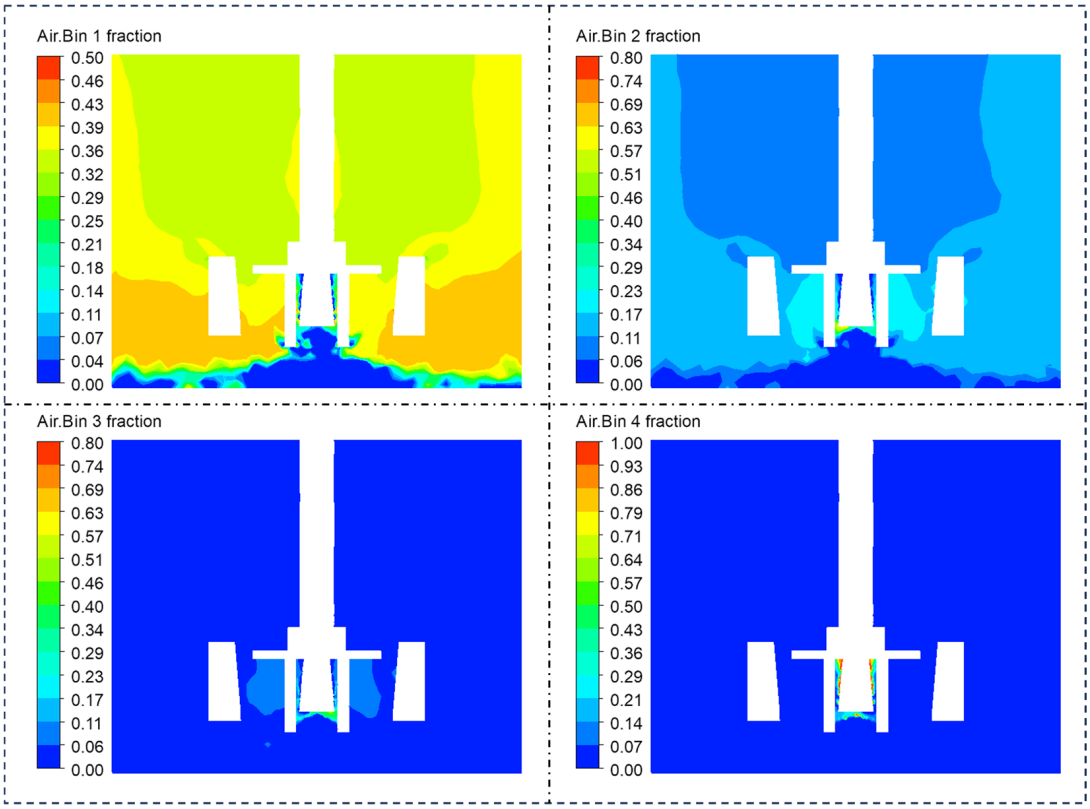

Figure 11. Volume fraction contours of bubbles with four diameters (Bin 1 to Bin 4) in the flow field under the +5° condition.

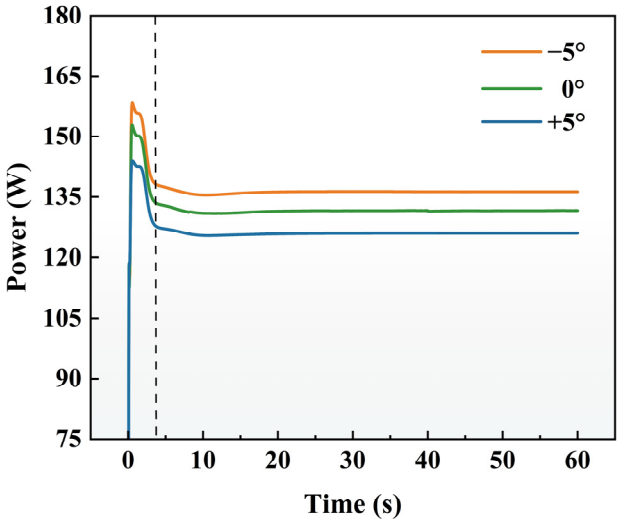

Figure 12. Variation curves of power over time under different taper angles.

The impeller and stator are the core components for energy input and flow field control in flotation machines. Their surface pressure distribution directly determines the structural fatigue life, wear rate, and operational stability. Therefore, analyzing the pressure distribution on the surfaces of the impeller and stator under different taper angles is of great significance for optimizing structural design and ensuring the stability of flotation operations. Figure 13 shows the pressure distribution on the impeller and stator under different taper angles. It can be seen from the figure that under the three taper angles, the pressure distribution on the impeller and stator exhibits localized high pressure and a distinct pressure gradient. The high-pressure zone on the stator is

mainly distributed on the pressure side inside the stator blades, with the impact concentrated in the middle of the blade leading edge. The pressure distribution on the stator surface varies only slightly among the three operating conditions. The high-pressure region of the impeller is mainly concentrated at the windward side of the blade outer edges. Under the three conditions of −5°, 0°, and +5°, the local maximum pressures reach 6317 Pa, 6280 Pa, and 6327 Pa, respectively, and the pressure gradually decreases radially inward. The pressure distribution on the impeller surface under the −5° and 0° conditions is relatively similar, while under the +5° condition, both the pressure side and suction side exhibit lower pressure in the inner region of the blade, accompanied by a larger pressure gradient, indicating stronger flow field disturbance and localized impact under this structural configuration.

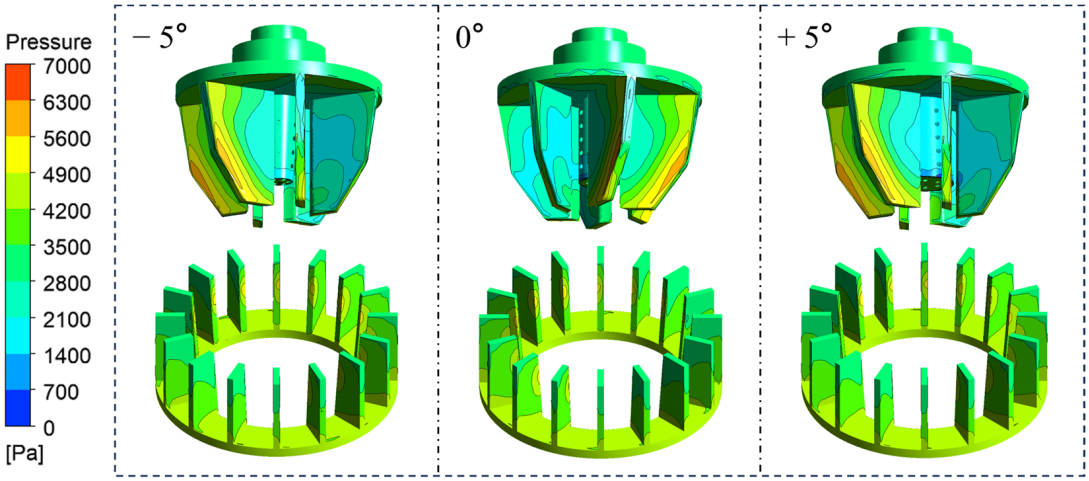

Figure 13. Pressure distribution on the impeller and stator under different taper angles.

A comparison of various indicators under different taper angle conditions is presented in Table 4. The +5° condition exhibits better performance in terms of gas holdup, bubble size, and power consumption, indicating higher flotation efficiency and energy savings. However, the intensified local pressure gradient of its impeller also leads to an accelerated wear rate of the blade surface and a shortened fatigue life, thereby increasing equipment maintenance costs. In actual production, while maintaining the advantages of the +5° taper structure, measures such as applying surface strengthening treatments, welding wear-resistant layers, or coating wear-resistant coatings can be adopted for the high-impact areas of the impeller blades to enhance the wear resistance of key components, thereby ensuring flotation performance and extending the service life of the equipment.

Table 4. Comparison of various indicators under different taper angle conditions.

	Flow Field Streamlines	Impeller Circulation Rate	Turbulent Kinetic Energy	Gas Holdup	0.5 mm Effective Bubble Count	Steady-State Operating Power	Impeller, Stator Pressures
−5°		0.074 m^3/s	0.02638 m^2/s^2	11.2%	1,960,431	136.3 W	6317 Pa
0°		0.072 m^3/s	0.032 m^2/s^2	14.1%	2,411,505	131.6 W	6280 Pa
+5°	√	0.070 m^3/s	0.02435 m^2/s^2	19.2%	3,803,828	126.0 W	6327 Pa

4. Conclusions

This study investigates the KYF inflatable mechanical agitation flotation machine. Through CFD numerical simulation combined with the population balance model (PBM),

the effects of three taper angles of the air distributor (−5°, 0°, and +5°) on the internal flow field distribution, gas-phase characteristics, and stirring power consumption of the flotation machine are systematically explored. The following conclusions are drawn:

(1) The distribution characteristics of turbulent kinetic energy differ significantly under the three taper angles. The peak turbulent kinetic energy is concentrated in the shear zone between the impeller and stator. The peak value is highest under the 0° condition, at 0.032 m^2/s^2, and lowest under the +5° condition, at 0.02435 m^2/s^2. However, under the +5° condition, the vertical distribution of turbulent kinetic energy is the most uniform, and the turbulent kinetic energy is more evenly distributed across various regions of the flotation cell.

(2) The +5° condition exhibits the optimal gas-phase distribution characteristics. The peak gas holdup in the impeller-stator region reaches 19.2%, and the number of efficient bubbles with a diameter of 0.5 mm reaches 3.8×10^6 per m^3, which is significantly higher than under the other conditions. The number of microbubbles is positively correlated with turbulent kinetic energy. Under the 0° condition, excessive bubble breakup occurs due to high turbulent kinetic energy, thus resulting in a larger number of microbubbles.

(3) The spatial distribution of bubble size exhibits clear zoning characteristics. Efficient bubbles are mainly concentrated in the high-shear region between the impeller and stator, providing a sufficient gas–liquid interface for bubble–particle collision and attachment. Although large bubbles are less efficient in terms of attachment, they are widely distributed in the upper part of the flotation cell and serve as the main carrier for the upward transport of mineralized bubbles.

(4) Under the +5° condition, the power consumption during stable operation is the lowest, at 126.0 W, which is 7.557% and 4.255% lower than those under the −5° and 0° conditions, respectively. The high-pressure zone on the impeller is concentrated on the pressure side of the outer blade edge, while that on the stator is located on the pressure side of the inner blade surface. However, under this condition, the pressure gradient on the impeller surface is larger, which may accelerate blade wear. Measures such as surface strengthening treatments can be adopted to balance performance improvement with equipment durability.

The present study primarily conducts numerical simulations, in which the complex multiphase flotation process inside the flotation cell is simplified to a gas–liquid two-phase flow, without considering the effect of solid particles. Consequently, there is a certain simplification discrepancy compared with actual industrial conditions. Future research will introduce a discrete phase model to establish a gas–liquid–solid multiphase flow model that more closely represents actual operating conditions. Furthermore, the temperature field and a simplified chemical reaction model will be progressively coupled to investigate the influence of multiphysics fields on the flotation process, thereby further improving simulation accuracy and engineering applicability.

Author Contributions: Conceptualization, C.L. and H.Z. (Hongliang Zhao); methodology, C.L.; software, N.W.; validation, N.W. and M.W.; formal analysis, H.Z. (Hongliang Zhao); investigation, H.Z. (Hanwen Zhang); resources, C.L. and H.Z. (Hongliang Zhao); data curation, H.Q.; writing—original draft preparation, N.W.; writing—review and editing, H.Z. (Hanwen Zhang) and H.Q.; visualization, M.W.; supervision, C.L.; project administration, H.Z. (Hongliang Zhao); funding acquisition, C.L. All authors have read and agreed to the published version of the manuscript.

Funding: This research was funded by Open Foundation of State Key Laboratory of Mineral Processing (BGRIMM-KJSKL-2025-01).

Data Availability Statement: The original contributions presented in this study are included in the article. Further inquiries can be directed to the corresponding authors.

Conflicts of Interest: Author Chao Lv was employed by BGRIMM Technology Group. The remaining authors declare that the research was conducted in the absence of any commercial or financial relationships that could be construed as a potential conflict of interest.

References

1. Tan, M.; Shen, Z.; Yang, Y. Research progress of mineral processing equipment technology. *J. Green Mine* **2024**, *2*, 85–93. [CrossRef]
2. Yang, J.; Qing, L.; Zhang, J. Current Condition and Developing Tendency of Spodumene Beneficiation Processing. *Mod. Min.* **2022**, *38*, 28–31. [CrossRef]
3. Anzoom, S.J.; Bournival, G.; Ata, S. Coarse particle flotation: A review. *Miner. Eng.* **2024**, *206*, 108499. [CrossRef]
4. Yang, B.; Zhu, L.; He, J.; Yin, W.; Yao, J. A feasible strategy for depressant-free flotation separation of siderite from magnesiohornblende using a highly selective collector. *J. Mol. Liq.* **2024**, *394*, 123689. [CrossRef]
5. Ma, X.; Wen, P.; Fan, Y.; Dong, X.; Sun, W.; Min, F.; Feng, Z.; Xie, J. Quantitative analysis of high-efficiency dewatering under ultrahigh pressures: Moisture storage state and filter-cake pore structure. *Miner. Eng.* **2026**, *237*, 109969. [CrossRef]
6. Shen, Z.; Fan, X.; Liu, C.; Liu, G. Research Progress and Development Trend of Flotation Equipment. *Nonferrous Met. (Miner. Process. Sect.)* **2025**, *10*, 1–12. [CrossRef]
7. Sui, J.; He, D.; Li, Z.; Zhang, Z.; Liang, H.; Rashid, H. Current status of application of flotation machine and prospect. *Ind. Miner. Process.* **2021**, *50*, 53–58. [CrossRef]
8. Li, Q.; Shen, Z. In-Situ Detection Technology for Bubble Characteristics in Flotation Kinetics Process. *Copp. Eng.* **2024**, *3*, 47–53. [CrossRef]
9. Zhang, H.; Tang, Z.; Xie, Y.; Gao, X.; Chen, Q.; Gui, W. Long short-term memory-based grade monitoring in froth flotation using a froth video sequence. *Miner. Eng.* **2021**, *160*, 106677. [CrossRef]
10. Draw, M.; Rzehak, R. A flotation framework for Eulerian multiphase CFD: Integrating bubble-particle aggregates and flotation kinetics. *Miner. Eng.* **2025**, *228*, 109258. [CrossRef]
11. Kim, M.; Kim, K.; You, K. Numerical analysis on the shear effect of the clearance of the stator and rotor in a tank-type flotation cell. *Miner. Eng.* **2023**, *191*, 107970. [CrossRef]
12. Lv, C.; Ji, Z.; Yang, T.; Zhao, H.; Zhang, H. Numerical simulation of deformation and breakage of compound droplet in air flow. *Phys. Fluids* **2024**, *36*, 023306. [CrossRef]
13. Zhao, Z.; Shi, S. Numerical Simulation Study on the Stator Optimization of XCF-50 m^3 Flotation Cell. *Nonferrous Met.* **2025**, *15*, 1006–1015. [CrossRef]
14. Fan, X.; Hu, S.; Shi, S. CFD Analysis of Stator Key Parameters in KYF Flotation Cell and Their Impact Mechanisms on Monophasic Flow Field Performance. *Nonferrous Met. (Miner. Process. Sect.)* **2025**, *8*, 103–114. [CrossRef]
15. Wu, F.; Sun, W.; Shi, S.; Dong, G.; Duan, L. Simulation Researchon Big Nozzle Sparger Aerating Performance. *Nonferrous Metall. Equip.* **2023**, *37*, 20–25. [CrossRef]
16. Gao, S.; Meng, L.; Wei, D.; Zhao, Q.; Wang, X.; Hou, D. Influence of the impeller diameter and off-bottom clearance on the flow velocity distribution characteristics near the bottom inside a flotation machine. *Minerals* **2020**, *11*, 31. [CrossRef]
17. Xu, H.; Shi, Y.; Li, H.; Jang, L.; Gao, H. Effect of short blade impeller on the performance of flotation machine based on CFD-PBM model. *Clean Coal Technol.* **2024**, *30*, 593–597. [CrossRef]
18. Li, C. Optimization design of iron ore flotation machine impeller parameters based on fluid mechanics. *China High-Tech* **2025**, *16*, 42–44. [CrossRef]
19. Niu, F.; Dou, N.; Zhang, J. Effect of Impeller Speed and Particle Size on Solid-Liquid Two-Phase Flow Field Characteristics of Flotation Machine. *Min. Metall. Eng.* **2025**, *45*, 77–83. [CrossRef]
20. Pan, J.; Niu, H.; Zhou, C.; Peng, C.; Cong, L.; Shi, S.; Wen, Z. Structure optimization of pneumatic micro-bubble flotation machine based on numerical simulation. *Miner. Eng.* **2025**, *232*, 109547. [CrossRef]
21. Shen, Z.; Zhang, M.; Shi, S.; Zhang, Y.; Duan, L. The scale-up and dynamics performance research on the air forced self pumping flotation cell. *J. China Univ. Min. Technol.* **2022**, *51*, 434–444. [CrossRef]
22. Ren, B.; Shen, Z.; Shi, S.; Zhang, M.; Sun, W. Research on XCF Flotation Machine Performances Based on Experiment and Simulation. *Nonferrous Met. (Miner. Process. Sect.)* **2022**, *2*, 129–136. [CrossRef]
23. Jin, Y.-S.; Sun, W.; Peng, J.; Shen, Z.-C.; Han, H.-S.; Sun, L.; Xiao, Y.; Luo, Y.-J.; Chen, Y. Effects of operating parameters on size and distribution of bubbles in coarse-particle flotation column. *Trans. Nonferrous Met. Soc. China* **2025**, *35*, 3120–3133. [CrossRef]
24. Tan, M.; Shen, Z.; Zhang, F. Dynamics performance of a new type of flotation machine rotor and its effect on coarse particles flotation performance. *Nonferrous Met. Sci. Eng.* **2022**, *13*, 93–100. [CrossRef]

25. Yu, X.; Li, B.; Niu, F.; Zhang, J.; Chang, Z.; Wei, L.; Tong, S. Study on the effect of flow field optimization on flotation efficiency. *Int. J. Coal Prep. Util.* **2025**, *45*, 128–145. [CrossRef]
26. Prakash, R.; Majumder, S.K.; Singh, A. Flotation technique: Its mechanisms and design parameters. *Chem. Eng. Process. Process Intensif.* **2018**, *127*, 249–270. [CrossRef]
27. Zhou, J.; Mao, Z.; Yuan, X.; Shi, S. Mechanism Research of Bubble Breaking in KYF Flotation Machine. *Nonferrous Met. (Miner. Process. Sect.)* **2024**, *7*, 55–61. [CrossRef]
28. Lv, C.; Chen, X.-X.; Ji, Z.-X.; Zhao, H.-L.; Yang, T.; Yu, L.-H. Simulation of bubble breaking process in a jet mixing reactor for desulfurization of molten iron. *J. Iron Steel Res. Int.* **2023**, *30*, 1117–1127. [CrossRef]
29. Liu, P.; Diao, Z.; Yang, X.; Zhang, Y.; Zhang, J.; Wang, H. Study on the mass transfer characteristics of gas and liquid phases in a three-layer combined paddle fermenter. *J. Environ. Chem. Eng.* **2022**, *10*, 108791. [CrossRef]
30. Gu, D.; Wen, L.; Xu, H.; Ye, M. Study on hydrodynamics characteristics in a gas-liquid stirred tank with a self-similarity impeller based on CFD-PBM coupled model. *J. Taiwan Inst. Chem. Eng.* **2023**, *143*, 104688. [CrossRef]
31. Gao, S.; Xu, Y.; Li, J.; Ye, S.; Huang, W. Simulation study of microbubbles' break-up and coalescence in centrifugal pump based on TFM-PBM coupling model. *CIESC J.* **2021**, *72*, 5082. [CrossRef]
32. Sun, W. *Analysis of Gas-Liquid Dispersion Characteristics and Factors of KYF-0.2 Flotation Machine by CFD Method*; Beijing University of Chemical Technology: Beijing, China, 2020. [CrossRef]

Disclaimer/Publisher's Note: The statements, opinions and data contained in all publications are solely those of the individual author(s) and contributor(s) and not of MDPI and/or the editor(s). MDPI and/or the editor(s) disclaim responsibility for any injury to people or property resulting from any ideas, methods, instructions or products referred to in the content.